

See discussions, stats, and author profiles for this publication at: <https://www.researchgate.net/publication/319917813>

Characterization of defects in copper antimony disulfide

Article in *Journal of Materials Chemistry A* · September 2017

DOI: 10.1039/C7TA07012H

CITATIONS

0

READS

34

7 authors, including:



Francisco Willian de Souza Lucas
Universidade Federal de São Carlos

19 PUBLICATIONS 48 CITATIONS

[SEE PROFILE](#)



Haowei Peng
Temple University

58 PUBLICATIONS 1,070 CITATIONS

[SEE PROFILE](#)



Lucia Mascaro
Universidade Federal de São Carlos

94 PUBLICATIONS 1,126 CITATIONS

[SEE PROFILE](#)



Andriy Zakutayev
National Renewable Energy Laboratory

114 PUBLICATIONS 1,496 CITATIONS

[SEE PROFILE](#)

Some of the authors of this publication are also working on these related projects:



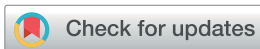
Rehabilitation of the Perdew-Burke-Ernzerhof generalized gradient approximation for layered materials [View project](#)



Construction, characterization and use of solid amalgam electrodes as sensor in electroanalysis [View project](#)

All content following this page was uploaded by [Francisco Willian de Souza Lucas](#) on 30 November 2017.

The user has requested enhancement of the downloaded file.



Cite this: DOI: 10.1039/c7ta07012h

Characterization of defects in copper antimony disulfide†

Francisco Willian de Souza Lucas,^a Haowei Peng,^a Steve Johnston,^a Patricia C. Dippo,^a Stephan Lany,^a Lucia H. Mascaro^b and Andriy Zakutayev^{id}*^a

Copper antimony disulfide (CuSbS₂) with the chalcocite structure is a promising photovoltaic (PV) absorber material with several excellent measured optoelectronic properties, such as a solar matched band gap and tunable hole concentration. However, much less is known from an experimental perspective about defects in CuSbS₂, even though the defects are critical for solar cell performance. Here, we explore the defect properties in CuSbS₂ thin film materials and photovoltaic devices using photoluminescence and capacitance-based spectroscopies, as well as first principles theoretical calculations. We measured three electrically and optically active acceptor defects in CuSbS₂, and assigned them to the copper vacancies, sulfur vacancies, and/or copper on antimony antisites by comparison with theoretical calculations. Their activation energies, concentrations, and capture cross sections have been determined and compared to other chalcogenide absorber materials. These fundamental parameters should enable more accurate simulations of CuSbS₂ PV devices, paving the way for future improvements in CuSbS₂ solar cell efficiencies.

Received 9th August 2017
Accepted 16th September 2017

DOI: 10.1039/c7ta07012h

rsc.li/materials-a

1. Introduction

Copper antimony disulfide (CuSbS₂), with the chalcocite crystal structure, is an emerging non-toxic and earth-abundant photovoltaic (PV) absorber material. It features an optical absorption coefficient larger than 10⁵ cm⁻¹ at 1.8 eV,¹⁻³ a slightly indirect band gap of 1.4–1.5 eV,¹⁻⁵ tunable hole concentrations in the range of 10¹⁶ to 10¹⁸ cm⁻³, and a hole mobility of 0.1–1.0 cm² V⁻¹ s⁻¹ in polycrystalline thin films.^{1,2} Despite these promising basic optoelectronic properties, there are few experimental studies of other PV-relevant properties related to defect concentration and carrier recombination. A better understanding of these properties is crucial for an enhanced efficiency of CuSbS₂ thin-film solar cells.

The current highest efficiency of CuSbS₂ thin-film solar cells is only 3.13%⁴ (close to 1% from several other reports^{2,6,7}), comparable to the almost 5% efficiency of isostructural CuSbSe₂ devices.⁶ What are the limiting factors for these relatively low efficiencies? Some researchers argued that well-defined ohmic contacts could improve the CuSbS₂ device efficiency.² Others proposed the large band-offset between the absorber and the commonly used CdS contact layer as one of the limiting factors.^{6,7} Yet another group has shown, by calculating the

defect formation enthalpies, that copper vacancies (V_{Cu}) are the defects that control the p-type conductivity in CuSbS₂, and documented the calculated formation enthalpies of other possible defects.³ However, understanding of how these defects can limit the device performance, and detailed experimental defect characterization of this material are missing from the literature.

There are many advanced material- and device-characterization techniques to study the influence of defects on the performance of photovoltaic devices. For example, photoluminescence (PL) spectroscopy can be used to observe radiative transitions associated with defects in semiconductors.^{8,9} Combining the PL measurement with first-principles calculations further enables attributing the PL transitions to specific defects.¹⁰⁻¹⁴ PV-device characterization techniques based on capacitance–voltage measurements are another set of powerful methods. Admittance spectroscopy (AS) provides insight into the energetic position and the density of states of the defects.⁸ Deep level transient spectroscopy (DLTS) enables quantification of the defect type (donor or acceptor), activation energies, defect concentrations, and capture cross sections.¹⁵

Here, we investigate the defect properties in the CuSbS₂ material from both experimental and computational perspectives of this material, as well as from experimental characterizations of CuSbS₂-based PV-devices. We prepared and characterized three types of CuSbS₂ material samples: as-deposited and annealed CuSbS₂ thin films on glass and molybdenum/soda-lime glass (Mo/SLG) substrates; CuSbS₂ micro-crystals grown on a Mo/SLG substrate; and CuSbS₂ solar

^aNational Renewable Energy Laboratory, Golden, CO 80401, USA. E-mail: andriy.zakutayev@nrel.gov

^bFederal University of Sao Carlos, São Carlos, SP 13565-905, Brazil

† Electronic supplementary information (ESI) available. See DOI: 10.1039/c7ta07012h

cell devices based on the annealed thin-film samples. Our study spans from macroscopic capacitance-based measurements of the defects present in the PV device, to microscopic evaluation of the radiative behavior of these defects by temperature- and power-dependent photoluminescence in thin films, and to atomic-scale defect identification by first-principles calculations. Combining the results from all of these techniques, we propose a model of defect levels within the band gap for CuSbS_2 . We expect this new fundamental understanding of defect physics in CuSbS_2 to aid future improvements in efficiencies of CuSbS_2 -based solar cells.

2. Methods

CuSbS_2 films were deposited by the self-regulated growth approach,^{1,16} using the radio frequency (RF) magnetron co-sputtering of one 5 cm-diameter Cu_2S and two 5 cm-diameter Sb_2S_3 targets (99.999%) with a power of 40 W applied to each. The same chamber conditions were used to grow $\text{Cu}_2\text{S}/\text{Mo}/\text{soda lime glass (SLG)}$ precursor thin films, but only using the Cu_2S target. Deposition of the phase-pure stoichiometric CuSbS_2 films was performed in 3 mTorr of argon (99.99%) in a 40 L vacuum chamber with a base pressure of 10^{-7} Torr on a $5 \times 5 \text{ cm}^2$ Mo/SLG substrate. The resulting film thickness was in the range of 1.4–1.6 μm . More details of the CuSbS_2 thin film deposition process have been reported previously.¹

Thermal treatment (TT) was performed in a one-zone tube furnace under a N_2 atmosphere rich in Sb_2S_3 vapor at 455 °C for 11h, following the previously reported optimized conditions.¹⁷ The CuSbS_2 crystals supported on Mo/SLG films were grown by annealing a $\sim 500 \text{ nm}$ Cu_2S film under the conditions of the aforementioned TT. For simplification, the microcrystals supported on Mo/SLG will be referred to as “crystals” in the following text. Both the films and the crystals were subjected to a selective chemical etch for the removal of the Sb_2S_3 secondary phase that could be formed during thermal treatment, as described in our prior publication.¹⁷ PV devices with the $\text{Mo}/\text{p-CuSbS}_2/\text{n-CdS}/\text{i-ZnO}/\text{ZnO}/\text{Al}/\text{Al}$ architecture were fabricated from annealed films (TT-11h) by chemical bath deposition of CdS, RF sputtering of intrinsic/conductive transparent $\text{i-ZnO}/\text{ZnO}/\text{Al}$, and e-beam evaporation of aluminum grids, as described elsewhere.^{6,7,17,18}

Phase identification of the films and the crystals was performed by X-ray diffraction (XRD) (Bruker D8 Discover). The composition and thickness of the pre- and post-thermally treated films (pre-TT and TT-11h, respectively) were determined by X-ray fluorescence (XRF) (Fischerscope® X-ray XDV®-SDD, Helmut Fischer GmbH). The carrier concentration was evaluated by Hall effect measurements (Accent HL5500PC®) using the van der Pauw resistance configuration at room temperature.

Photoluminescence (PL) experiments on films (as-grown and annealed) and on crystals were performed in a helium closed-cycle cryostat. Excitation dependent PL experiments were performed at 4.25 K with laser powers from 0.1 to 16 mW. The temperature-dependent experiments were performed from 4.25 K to room temperature (RT). A HeNe laser ($\lambda = 632.8 \text{ nm}$ or $E_g = 1.960 \text{ eV}$) was used for excitation, with a 5 second exposure time,

a 280 μm slit, and a 695 nm-long pass filter. The PL spectra were collected by using a spectrometer with a diffraction grating of 600 grooves/mm and a 1024×256 pixel charge coupled device (CCD). The PL spectra were analyzed by fitting the measured spectra to Gaussian curves.

Admittance Spectroscopy (AS) and deep-level transient spectroscopy (DLTS) studies were performed on devices with the architecture of $\text{Mo}/\text{p-CuSbS}_2/\text{n-CdS}/\text{i-ZnO}/\text{ZnO}/\text{Al}/\text{Al}$, prepared as described above. Capacitance–voltage measurements were carried out using an Agilent 4294A precision impedance analyzer. The frequency was varied from 1 kHz to 1 MHz, and the temperature swept from 315 K to 15 K. The DC bias voltage was swept from 1.0 V reverse bias to 0.2 V forward bias.¹⁹ DLT spectra were measured using a commercial DLTS system that used Fourier transform to characterize the transients at a reverse bias voltage (V_R) of -2 V , a trap-filling pulse (V_P) of 0 V, and saturation pulse widths (t_P) of 10 μs and 100 ms.²⁰

The commonly used supercell approach²¹ was used to explore the defect physics in CuSbS_2 . The first-principles calculations were performed with the Vienna *ab initio* simulation package (VASP),^{22,23} using the projected augmented wave (PAW) method^{24,25} implemented therein. The standard Perdew–Burke–Ernzerhof (PBE) generalized gradient approximation to the exchange correlation was chosen,²⁶ and an on-site Hubbard $U = 5 \text{ eV}$ was applied to the Cu d orbitals to reduce the self-interaction-error.²⁷ A 96-atom supercell was used to model the defect systems, with the lattice vectors fixed to the pure phase. The errors related to the finite supercell size, band gap and elemental reference energy were corrected according to prior literature reports.^{28,29}

3. Results and discussion

The pre- and post-thermally treated films (pre-TT and TT-11h, respectively), as well as the crystals, are phase-pure orthorhombic CuSbS_2 , as shown in the X-ray diffraction (XRD) patterns in Fig. S1, ESI.† Based on the XRF characterization, we also conclude that the thermal treatment does not change the stoichiometry or thickness of the films. The crystals and pre-TT and TT-11h films maintain a slightly Cu-poor composition with a ratio of $\text{Cu}/(\text{Cu} + \text{Sb}) = 0.48$, within the error of the XRF measurement compared to the nominal CuSbS_2 stoichiometry. The Hall effect shows that the hole concentrations of the pre-TT and TT-11h films are mid- 10^{16} and 10^{17} cm^{-3} , respectively. However, PV devices made with the TT-11h films surprisingly show only a slight increase in their efficiency compared to the one made with non-annealed films, while the significant improvements in the morphology and optoelectronic properties due to the thermal treatment⁷ would suggest a much better performance of the TT-11h device. This unexpected behavior encouraged us to find the defects that may limit the device performance.

3.1 Admittance and deep-level transient spectroscopies

To characterize the TT-11h film by AS and DLTS, devices of the $\text{Mo}/\text{p-CuSbS}_2/\text{n-CdS}/\text{i-ZnO}/\text{ZnO}/\text{Al}/\text{Al}$ architecture were made,

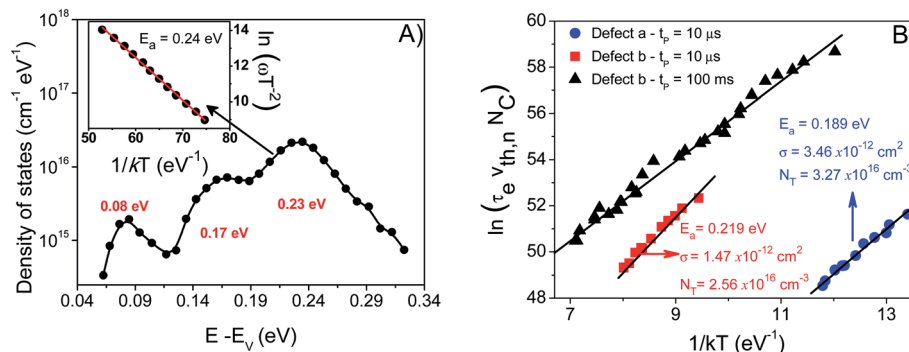


Fig. 1 (A) Density of defect states *versus* energy obtained from the admittance spectroscopy. The inset shows the Arrhenius plot of the peak at about 0.23 eV. (B) Arrhenius plot from DLTS measurements at saturation pulse widths (t_p) of 10 μ s and 100 ms. The values of the activation energy (E_a), capture cross section (σ) and effective density of trap states (N_T) for each defect are also shown.

as previously described.^{7,17,18} From AS (Fig. 1A), we observed the presence of three electronic defects: a shallow one at about 0.08 eV, and two deeper ones at 0.17 eV and 0.24 eV above the valence band maximum. The corresponding densities of defect states are 10^{15} cm^{-1} eV^{-1} and 10^{16} cm^{-1} eV^{-1} . The Arrhenius plot of the more abundant deeper defect showed a slope of -0.24 eV, corresponding to its activation energy (Fig. 1A, inset). Previous defect calculations³ suggest the shallow transition at 0.08 eV to be associated with the copper vacancy (V_{Cu}), but experimental support for this assignment is needed. Regardless, this shallow defect is unlikely the limiting factor to the CuSbS_2 solar-cell device performance. Instead, the two transitions close to 0.2 eV related to deeper defects may be more detrimental.

To study the two deeper defects, we performed temperature-dependent DLTS, with the results shown in Fig. 1B for two different saturation pulse widths (t_p) of 10 μ s and 100 ms. The activation energies of the deeper defects are approximately 0.19 and 0.22 eV from the short 10 ms saturation DLTS, similar to those from the 100 ms saturation result (Fig. 1B inset), and close to the results obtained by AS. From the sign of the DLTS signal (not shown here), we could also conclude that these deep defects are hole traps (acceptors). The capture cross section (σ) and effective density of trap states (N_T) for each defect were

determined to be $1.5\text{--}3.5 \times 10^{-12}$ cm^{-2} and $2.6\text{--}3.3 \times 10^{16}$ cm^{-3} , of which the latter is in reasonable agreement with the results from AS. These results are similar to those of CuSbS_2 ,²¹ and can be used for future CuSbS_2 photovoltaic device performance simulations.

3.2 Photoluminescence spectroscopy

The results of AS and DLTS measurements together indicate that there are both shallow and deep defects that may influence the performance of the PV devices with thermally treated CuSbS_2 absorbers. For more information on the microscopic origin of these defects, three types of CuSbS_2 films with different preparation conditions were characterized: the as-deposited films, thermally treated films, and microcrystals. For each sample, we performed photoluminescence spectroscopy measurements, evaluating the temperature and the excitation power dependencies of the radiative defect signatures.

Fig. 2 shows the normalized PL spectra at 4.25 K and a laser power of 2.2 mW for the three samples (Fig. 2A) and the deconvolution of the TT-11h PL spectrum (Fig. 2B). The film samples show two visible peaks at about 1.29 and 1.50 eV, with a little shoulder at about 1.34 eV. Meanwhile, the crystals show a peak at around 1.50 eV, with a negligible contribution of the peak at about 1.29 eV (inset in Fig. 2A). Since the wide peak at

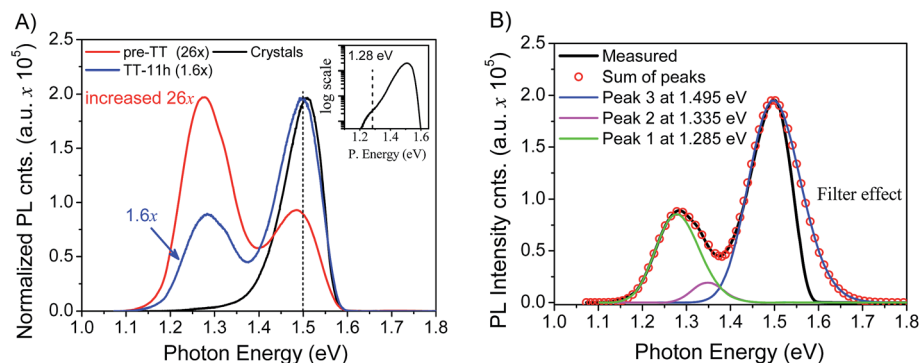


Fig. 2 (A) Normalized PL spectra of the crystals and pre-TT (increased 26 \times) and TT-11h (increased 1.6 \times) films at 4.25 K and a laser power of 2.2 mW. The inset shows the crystal spectrum on a logarithmic scale. (B) Deconvolution of the TT-11h PL spectrum (increased 1.6 \times). The asymmetric shape observed for peak 3 was caused by filter cut-off.

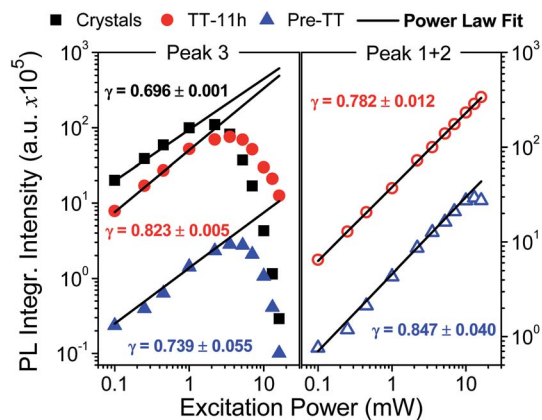


Fig. 3 PL integrated intensity as a function of excitation power for peak 3 (filled symbols, left side) and the sum of peaks 1 and 2 (unfilled symbols, right side). Black squares, blue triangles, and red circles represent the crystals and pre-TT and TT-11h films, respectively. The solid lines are the power law fit, following eqn (1).

around 1.29 eV has an evident shoulder at about 1.34 eV (Fig. 1A), the PL spectra were deconvoluted for estimating the position and intensity of each contribution. As shown in Fig. 2B, the PL spectra of the CuSbS_2 films are deconvoluted into three Gaussian-like peaks at about 1.29 eV (peak 1), 1.34 eV (peak 2), and 1.50 eV (peak 3). Since the CuSbS_2 band gap at 4.25 K is 1.58 eV,³⁰ these peaks (1, 2 and 3) are ~ 0.29 , ~ 0.24 and ~ 0.08 eV below the band-gap. These energies from the PL of the CuSbS_2 materials (Fig. 2b) agree reasonably well with those from the AS and DLTS of the CuSbS_2 devices (Fig. 1). We conclude that they originate from the same defects.

Since the de-convolution of peaks 1 and 2 is not unambiguous enough, we subsequently analyze them together (peak 1 + 2). Comparing the spectra of different thin-film samples in Fig. 2A, we find that the TT-11h film has a higher ratio between peaks 3 and 1 + 2 and also a 16-times higher intensity for peak 3 compared to the pre-TT film. This means that the annealed film has a lower concentration of defects associated with peak 1 + 2 and fewer non-radiative centers. The fact that peak 1 + 2 decreases and almost disappears when the material goes from pre-TT through TT-11h to crystals makes us believe that the

associated defects are progressively eliminated with the increase of the sulfur and antimony chemical potentials, promoted by thermal treatment in Sb_2S_3 vapor. This observation suggests that the chemical origin of these defects is related to Sb and S deficiency in the as-deposited CuSbS_2 thin-film sample.

3.3 Power-dependent photoluminescence

Fig. 3 shows the integrated PL intensity of peak 3 (left side) and of the sum of peaks 1 and 2 (right side) as a function of the excitation laser power, along with the power law fit of the data. The integrated PL intensity can be fitted by the following power law:³¹

$$I_{\text{PL}} \propto P^\gamma \quad (1)$$

where I_{PL} is the integrated PL intensity and P is the excitation laser power. The dimensionless exponent γ is known to be $1 < \gamma < 2$ for free-exciton or bound-exciton recombination, and $\gamma < 1$ for free-to-bound (FB) or donor-acceptor pair (DAP) recombination luminescence.³¹ The spectra at different laser powers for the crystals and TT-11h films can be seen in Fig. S2, ESI†

In Fig. 3, all peaks show $\gamma < 1$, and hence these processes can be associated with FB or DAP recombination. For DAP recombination, the energy of the peaks should shift significantly as the laser power increases.^{8,9} As shown in the derivative of intensity as a function of energy (Fig. S2†), the peak shift is < 4 meV dec^{-1} for peak 3 and < 2 meV dec^{-1} for peak 1 + 2, indicating that these processes cannot be related to DAP recombination; thus, they may be related to the FB recombination. This low peak shift also indicates that potentials that are known to be deleterious for the solar cell performance^{32–34} are small in CuSbS_2 .

In addition to the power law dependence at low excitation powers, a sharp decrease of peak 3 intensity is observed at an excitation power higher than 2.2 mW (left side of Fig. 3). The quenching behavior of peak 3 is not observed for peak 1 + 2. We relate this quenching behavior to the local heating up of the samples at a high laser excitation: since peak 3 can be associated with a very shallow trap that has a relatively low density (Fig. 1A), a small elevation of temperature can promote the thermal activation of this defect. Supporting this hypothesis,

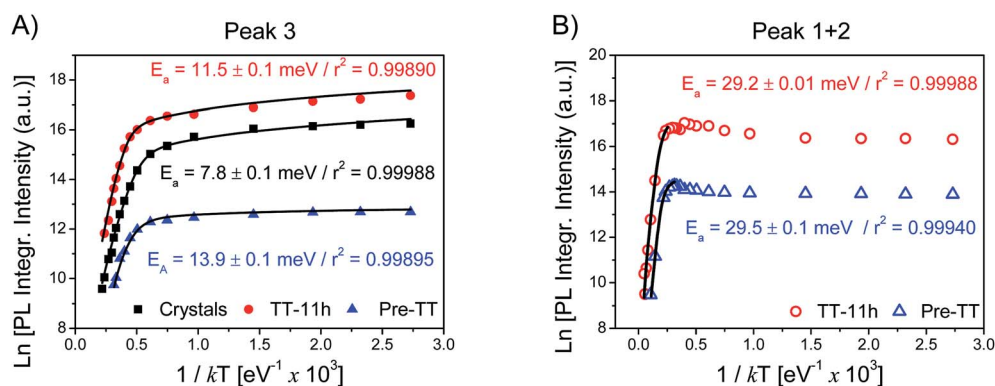


Fig. 4 PL integrated intensity versus $(kT)^{-1}$ for (A) peak 3 (filled symbols) and (B) sum of peaks 1 and 2 (unfilled symbols). Square, triangular, and circular symbols represent crystals and pre-TT and TT-11h films, respectively. The solid lines represent the Arrhenius fit, following eqn (2).

the crystals show a more abrupt quenching behavior, because thermal dissipation is more difficult in the isolated thicker (~ 3 to $5 \mu\text{m}$ tall) crystals than in the uniform films (thickness of $\sim 1.5 \mu\text{m}$). The surface and cross-sectional SEM images of these films can be seen in Fig. S3 in the ESI.† A similar PL quenching behavior has also been observed in $\text{Cu}_2\text{ZnSnS}_4$ polycrystals.³⁵

3.4 Temperature-dependent photoluminescence

Fig. 4A and B show the temperature dependent PL intensity of peak 3 and peak 1 + 2, respectively. The PL intensity dependence as a function of temperature for a free-to-bound recombination can be fitted using the following equation,^{9,36,37}

$$I_{\text{FB}}(T) = \frac{A T^{-\alpha}}{1 + (N_{\text{v}}^*/p)T^{3/2} \exp(-E_{\text{a}}/kT)} \quad (2)$$

where A is a constant, $N_{\text{v}}^* = 2(2\pi m_{\text{h}}k/h^2)^{3/2}$ is the density of states, m_{h} is the hole effective mass, h is the Planck constant, p is the hole concentration, E_{a} is the ionization energy (activation energy), k is the Boltzmann constant, and T is the absolute temperature. The PL spectrum dependence on temperature for the TT-11h film is shown in Fig. S4 in the ESI.†

From these results, one can conclude that for all samples the PL peaks show a common quenching behavior as the temperature increases (or kT^{-1} decreases). This trend can be associated with the thermal dissociation of the respective radiative centers and with the increase of non-radiative recombination. We also observe a small increase in the PL emission intensity for peak 1 + 2 at $(kT)^{-1} \sim 0.5 \times 10^3 \text{ eV}^{-1}$ with increasing temperature. This phenomenon is due to the redistribution of the carriers with the quenching of peak 3.³⁸ From Fig. 4, we note that the PL integrated intensity has a low rate of quenching in the low-temperature region, whereas above 19 K (for peak 3) and 40 K (for peaks 1 and 2), it decreases abruptly with increasing temperature. Peak 3 is totally quenched at about 40 K for all films, while peak 1 + 2 thermalizes at around 140 K and 230 K for pre-TT and TT-11h, respectively.

The defect ionization energies E_{a} and the ratio of the density of states to the hole concentration N_{v}^*/p can be estimated from the fitting of Fig. 4 data using eqn (2). The exponent “ α ” can be deduced from the low-temperature region, where the exponential term can be neglected so that $\log(I_{\text{FB}}(T))$ becomes linear to $-\alpha \log(T)$ (the hole concentration can be assumed to be constant in the temperature range of fitting). The straight line region at low temperature for the relation $\log(I_{\text{FB}}(T))$ versus $\log(T)$ for all peaks and samples shows a slope of 0.33, leading to the E_{a} and N_{v}^*/p values summarized in Table 1. The E_{a} for peak 1 + 2 of the films was around 29 meV, close to the 22.9–24.8 meV value observed for an acceptor level in Cu_2SnS_3 .³¹ The presence of defects/peak 1 + 2 also has a slight effect on the stability of the defect/peak 3, with E_{a} ranging from 7.85 to 13.95 meV.

Comparing the pre-exponential factor N_{v}^*/p of the two types of thin films presented in Table 1, we conclude that the hole concentration in the TT-11h film is about two times higher than in the pre-TT film. This agrees with our Hall effect measurement⁶ of 10^{17} cm^{-3} and mid- 10^{16} cm^{-3} in the TT-11h film and in the pre-TT film, respectively. With these hole concentrations

Table 1 Values of ionization energy (E_{a}) and density of state/hole concentration (N_{v}/p) for defect states associated with peak 3 and peak 1 + 2. These values were obtained from eqn (2) fitting of the experimental data shown in Fig. 4

Sample	Peak 3		Peak 1 + 2	
	E_{a} (meV)	N_{v}/p	E_{a} (meV)	N_{v}/p
Crystals	7.85 ± 0.12	0.80 ± 0.06	—	—
Pre-TT	13.95 ± 0.09	2.62 ± 0.10	29.49 ± 0.12	1.85 ± 0.04
TT-11h	11.55 ± 0.09	1.24 ± 0.05	29.24 ± 0.01	0.88 ± 0.01

and the N_{v}/p results in Table 1, we can estimate the hole effective mass by using the equation $N_{\text{v}}^* = 2(2\pi m_{\text{h}}k/h^2)^{3/2}$. For the TT-11h film we estimate $m_{\text{h}} = 6.9 - 8.7m_0$, and for the Pre-TT film we estimate $m_{\text{h}} = 3.9 - 4.9m_0$, where m_0 is the mass of a free electron. These values are ~ 10 times higher than for CIGS,³⁹ and in good agreement with the theoretical CuSbS_2 defect calculations.³⁰

3.5 Band-to-band recombination

An interesting PL phenomenon observed in the higher temperature range (from 110 K to room temperature) deserves more attention. Specifically, we observed the appearance of a new peak (referred to as NP below) with energy close to the band gap. The energies of different peaks as a function of temperature, in comparison with the temperature dependence of the indirect band gap determined from optical absorption measurements,⁴⁰ are shown in Fig. 5. The PL spectra as a function of temperature in this 110–300 K range are given in Fig. S4B of the ESI.† The temperature dependence of the peak energy and band gap was fitted using the following empirical equation proposed by Varshni:⁴¹

$$E(T) = E_0 - \frac{AT^2}{B + T} \quad (3)$$

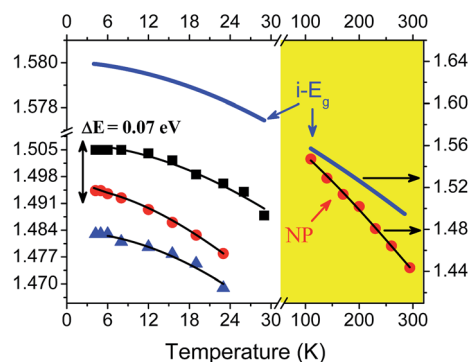


Fig. 5 Temperature dependence of the peak energy for peak 3 and the NP. Square, triangular, and circular symbols represent crystals and pre-TT and TT-11h films, respectively. The bold blue lines represent the temperature dependence of the indirect band gap ($i-E_{\text{g}}$) of the TT-11h film.⁴⁰ The solid lines represent the Varshni fit, following empirical eqn (3).

Table 2 Varshni empirical constants obtained from the eqn (3) fit of the experimental data shown in Fig. 5

Sample	A (meV K ⁻¹)	B (K)	E_0 (eV)	$E_0(i-E_g) - E_0$ (eV)
Indirect band-gap (i- E_g) TT-11h ⁴⁰	0.411	106	1.580	0.000
Crystals (peak 3)	0.414	179	1.506	0.074
Pre-TT (peak 3)	0.517	179	1.483	0.097
TT-11h (peak 3)	0.461	179	1.495	0.085
TT-11h (NP)	0.655	122	1.580	0.000

where A and B are empirical constants and E_0 is the energy gap at 0 K.

The best Varshni fit of the experimental data shown in Fig. 5 is achieved with the parameters summarized in Table 2. Since E_0 of the NP is equal to the observed E_0 of the indirect band gap, it is likely that this radiative process is due to a band-to-band recombination (BB). The occurrence of BB at high temperatures in polycrystalline materials is not uncommon. For example, it has also been observed in kesterites (such as CZTS³⁵) and chalcopyrites (such as AgGaTe₂ (ref. 42)). However, the appearance of the band-to-band recombination is quite remarkable for the CuSbS₂ material, since indirect-gap semiconductors usually show overall weak PL. From Table 2, we also observe that the crystals show a higher E_0 for peak 3, consistent with the lower ionization energy of the acceptor defect associated with this transition.

3.6 Defect theoretical calculations

The above analysis of the temperature- and power-dependent PL measurements for different CuSbS₂ samples provides additional insights into the characteristics of the defects observed in CuSbS₂ photovoltaic devices. For example, it is clear now that the deeper defects responsible for PL and AS/DLTS signals in the as-deposited samples are related to the Sb- and/or S-deficiency. To identify the likely atomic-scale origin of these defects, we performed the calculation of the formation enthalpy of different possible point defects that can be present in CuSbS₂

under the experimental S- and Sb-rich and Cu-poor processing conditions that correspond to thermal treatments.

The calculated room temperature hole concentration as a function of growth temperature (Fig. 6A) and the corresponding defect formation enthalpies as a function of Fermi level (Fig. 6B) are shown in Fig. 6. According to Fig. 6A, under the S-rich, Cu-poor, and Sb-rich conditions, the calculated hole concentration (10^{16} to 10^{17} cm⁻³) agrees well with the results of the Hall effect measurements. The plot of defect formation energies (Fig. 6B) confirms that the most abundant acceptor under the experimental Cu-poor (S-rich and Sb-rich) conditions is the copper vacancy (V_{Cu}). The V_{Cu} transition level ($-/0$) is very shallow, ~ 0.03 eV above the valence band maximum (VBM), in agreement with previous calculations of CuSbS₂ (ref. 3) and also with CuSbSe₂ defect calculation results.⁶ Copper on antimony antisites (Cu_{Sb}) is also an active acceptor defect, but with a higher formation energy and deeper transition levels (0.15 and 0.25 eV). The presence of V_{Sb} should be very rare, because its formation enthalpy (ΔH_f) is 2–3 eV higher than those of V_{Cu} and Cu_{Sb} under the p-type conditions.

The dominant donor defects are Cu interstitials (Cu_i). We have considered two different interstitial sites, one within the layer (Cu_{i-in}) and another one between the layers (Cu_{i-out}). Both of them are shallow donor defects (transition levels close to the conduction band minimum), with the latter having a slightly higher formation energy. The sulfur vacancies (V_{S-in} and V_{S-out}) also have relatively low ΔH_f . These vacancies have an amphoteric character, acting as a donor or an acceptor depending on the position of the Fermi level (E_F). The (0/+) transition level is around 0.15 eV for V_{S-out} and 0.35 eV for V_{S-in} , and the (2+/+) transition level is around 0.10 eV for V_{S-out} .

According to the results of our calculations, the position of the Fermi level in CuSbS₂ is determined by Cu_i donors and V_{Cu} acceptors. The equilibrium between these two defects sets the Fermi level (E_F) position at around 0.8 eV during the thermal treatment, where they intercept in Fig. 6B. It is important to note that at this E_F position, the formation enthalpy of the Cu_{Sb} and V_S defects is also comparable to that of V_{Cu} and Cu_i , so Cu_{Sb} and V_S may be present in substantial quantities. At room temperature, the equilibrium Fermi level drops to 0.5–0.6 eV above the valence band maximum.

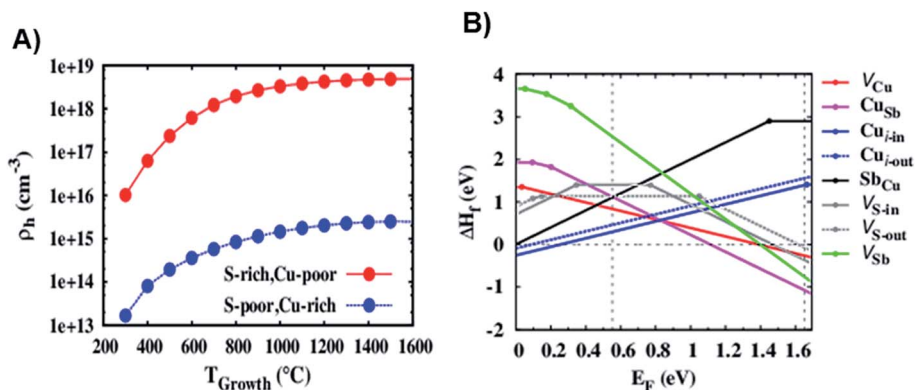


Fig. 6 Calculated (A) hole concentration under different synthesis conditions as a function of growth temperature, and (B) defect formation energies as a function of Fermi level (E_F), with vertical dashed line indicating equilibrium Fermi level.

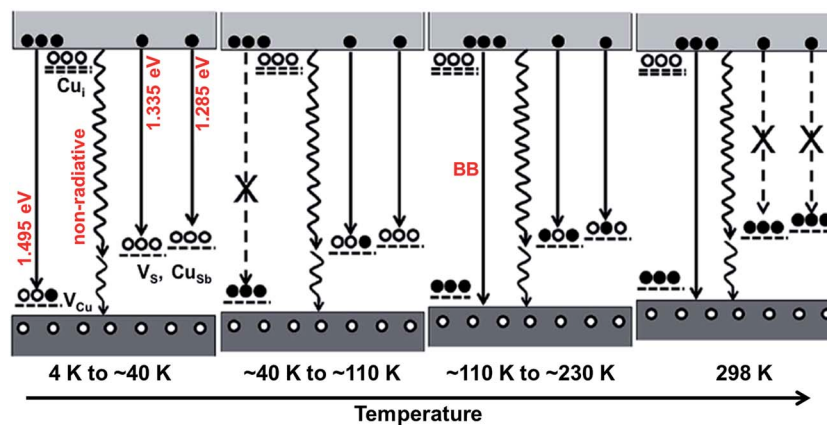


Fig. 7 Schematic energy diagram of the photoluminescence transitions observed for the TT-11h CuSb₂S₂ film in different temperature ranges. The upper light gray and bottom dark gray rectangles represent the conduction and valence bands, and the filled and unfilled circles represent the electrons and holes, respectively. The solid and dashed black arrows symbolize the active and quenched radiative recombinations respectively, while the wavy arrows are the non-radiative transitions. The likely defects are shallow V_{Cu} and Cu_i , as well as deeper V_S and Cu_{Sb} .

Based on these theoretical results, we propose that the deep acceptor signatures experimentally observed in the PL, AS and C-DLTS measurements result from Cu_{Sb} and/or V_S defects. This conclusion is consistent with the observation that the PL signatures of these defects are progressively eliminated with the increase of the sulfur and antimony chemical potentials, promoted by thermal treatment in Sb_2S_3 vapor. Such a proposed model for deep defects does not exclude the presence of Cu_i defects in $CuSbS_2$. It is likely that these shallow defects were completely ionized at all studied temperatures and saturation pulse widths, making their experimental observation difficult.

4. Summary and conclusions

The results of different experimental measurements (PL, AS, and DLTS) and theoretical calculations are summarized in the hypothetical CuSb₂S₂ defect diagram in Fig. 7. Based on this diagram we can also propose a simplistic mechanism that explains the appearing of the band-to-band (BB) recombination at increased measurement temperatures. The increase in temperature makes the neutral acceptor defects associated with the free-to-bound (FB) radiative channels thermally dissociate, donating holes to the valence band. In other words, as these acceptor defects become occupied by electrons that are thermally excited from the valence band, the photoexcited electrons in the valence band lose the ability to recombine through the corresponding free-to-bound (FB) radiative channels, and the BB radiative channel becomes progressively dominant. Fig. 7 shows this phenomenon as a function of temperature, taking as an example the experimental behavior of the TT-11h film. It is also worth mentioning that CuSb₂S₂ has a slightly indirect band-gap, which makes the phonon-assisted BB recombination have higher probability with increasing temperature.

In conclusion, we experimentally characterized different defects present in CuSb₂S₂ and identified their likely atomic origins with the aid of theoretical calculations. The AS, DLTS and PL results show three acceptor defects: a shallow one at

about 0.08 eV and two deeper ones at 0.17 eV and 0.24 eV above the valence band. Based on the results of the theoretical calculations, we propose that the defects at 0.08 eV are associated with V_{Cu} , and the ones at 0.17 eV and 0.24 eV are related to V_S and/or Cu_{Sb} acceptors. From the experimental results, we also estimated acceptor densities of $\sim 10^{16} \text{ cm}^{-3}$, capture cross sections σ of $\sim 10^{-12} \text{ cm}^{-2}$, and hole effective masses of $\sim 6.1m_0$, which can be used for CuSb₂S₂ photovoltaic device simulations. Overall, these results provide new insights into CuSb₂S₂ defects, which can aid future improvement in solar cells based on this emerging photovoltaic absorber.

Conflicts of interest

There are no conflicts to declare.

Acknowledgements

This work was supported by the U. S. Department of Energy, Office of Energy Efficiency and Renewable Energy, and Solar Energy Technology Program, under Contract No. DE-AC36-08GO28308 to NREL. For the execution of this work, F. W. S. L. was funded by the São Paulo Research Foundation (FAPESP), grant 2014/12166-3 and grant 2016/10513-3. We would like to thank Lauryn Baranowski and Adam Welch for providing the as-deposited CuSb₂S₂ samples and for useful technical discussions.

References

- 1 A. W. Welch, P. P. Zawadzki, S. Lany, C. A. Wolden and A. Zakutayev, *Sol. Energy Mater. Sol. Cells*, 2015, **132**, 499–506.
- 2 B. Krishnan, S. Shaji and R. Ernesto Ornelas, *J. Mater. Sci.: Mater. Electron.*, 2015, **26**, 4770–4781.
- 3 B. Yang, L. Wang, J. Han, Y. Zhou, H. Song, S. Chen, J. Zhong, L. Lv, D. Niu and J. Tang, *Chem. Mater.*, 2014, **26**, 3135–3143.

- 4 W. Septina, S. Ikeda, Y. Iga, T. Harada and M. Matsumura, *Thin Solid Films*, 2014, **550**, 700–704.
- 5 L. Shi, Y. Li, C. Wu and Y. Dai, *J. Alloys Compd.*, 2015, **648**, 507–511.
- 6 A. W. Welch, L. L. Baranowski, P. Zawadzki, S. Lany, C. A. Wolden and A. Zakutayev, *Appl. Phys. Express*, 2015, **8**, 82301.
- 7 F. W. de Souza Lucas, A. W. Welch, L. L. Baranowski, P. C. Dippo, H. Hempel, T. Unold, R. Eichberger, B. Blank, U. Rau, L. H. Mascaro and A. Zakutayev, *J. Phys. Chem. C*, 2016, **120**, 18377–18385.
- 8 M. A. Reshchikov and H. Morkoç, *J. Appl. Phys.*, 2005, **97**, 61301.
- 9 S. Levchenko, V. E. Tezlevan, E. Arushanov, S. Schorr and T. Unold, *Phys. Rev. B: Condens. Matter Mater. Phys.*, 2012, **86**, 45206.
- 10 J. Vidal, S. Lany, M. D'Avezac, A. Zunger, A. Zakutayev, J. Francis and J. Tate, *Appl. Phys. Lett.*, 2012, **100**, 32104.
- 11 A. Zakutayev, C. M. Caskey, A. N. Fioretti, D. S. Ginley, J. Vidal, V. Stevanovic, E. Tea and S. Lany, *J. Phys. Chem. Lett.*, 2014, **5**, 1117–1125.
- 12 A. Zakutayev, X. Zhang, A. Nagaraja, L. Yu, S. Lany, T. O. Mason, D. S. Ginley and A. Zunger, *J. Am. Chem. Soc.*, 2013, **135**, 10048–10054.
- 13 L. L. Baranowski, K. McLaughlin, P. Zawadzki, S. Lany, A. Norman, H. Hempel, R. Eichberger, T. Unold, E. S. Toberer and A. Zakutayev, *Phys. Rev. Appl.*, 2015, **4**, 44017.
- 14 L. L. Baranowski, P. Zawadzki, S. Lany, E. S. Toberer and A. Zakutayev, *Semicond. Sci. Technol.*, 2016, **31**, 123004.
- 15 S. Das, S. K. Chaudhuri, R. N. Bhattacharya and K. C. Mandal, *Appl. Phys. Lett.*, 2014, **104**, 192106.
- 16 A. W. Welch, L. L. Baranowski, F. W. de Souza Lucas, E. S. Toberer, C. A. Wolden and A. Zakutayev, in *2015 IEEE 42nd Photovoltaic Specialist Conference (PVSC)*, IEEE, 2015, pp. 1–4.
- 17 F. W. de Souza Lucas, A. W. Welch, L. L. Baranowski, P. C. Dippo, L. H. Mascaro and A. Zakutayev, in *2015 IEEE 42nd Photovoltaic Specialist Conference (PVSC)*, IEEE, 2015, pp. 1–5.
- 18 M. A. Contreras, M. J. Romero, B. To, F. Hasoon, R. Noufi, S. Ward and K. Ramanathan, *Thin Solid Films*, 2002, **403–404**, 204–211.
- 19 T. Walter, R. Herberholz, C. Müller and H. W. Schock, *J. Appl. Phys.*, 1996, **80**, 4411.
- 20 S. Weiss and R. Kassing, *Solid-State Electron.*, 1988, **31**, 1733–1742.
- 21 C. Freysoldt, B. Grabowski, T. Hickel, J. Neugebauer, G. Kresse, A. Janotti and C. G. Van de Walle, *Rev. Mod. Phys.*, 2014, **86**, 253–305.
- 22 G. Kresse and J. Furthmüller, *Phys. Rev. B: Condens. Matter Mater. Phys.*, 1996, **54**, 11169–11186.
- 23 G. Kresse and J. Hafner, *Phys. Rev. B: Condens. Matter Mater. Phys.*, 1994, **49**, 14251–14269.
- 24 P. E. Blöchl, *Phys. Rev. B: Condens. Matter Mater. Phys.*, 1994, **50**, 17953–17979.
- 25 G. Kresse and D. Joubert, *Phys. Rev. B: Condens. Matter Mater. Phys.*, 1999, **59**, 1758–1775.
- 26 J. P. Perdew, K. Burke and M. Ernzerhof, *Phys. Rev. Lett.*, 1996, **77**, 3865–3868.
- 27 S. L. Dudarev, G. A. Botton, S. Y. Savrasov, C. J. Humphreys and A. P. Sutton, *Phys. Rev. B: Condens. Matter Mater. Phys.*, 1998, **57**, 1505–1509.
- 28 H. Peng, D. O. Scanlon, V. Stevanovic, J. Vidal, G. W. Watson and S. Lany, *Phys. Rev. B: Condens. Matter Mater. Phys.*, 2013, **88**, 115201.
- 29 S. Lany and A. Zunger, *Phys. Rev. B: Condens. Matter Mater. Phys.*, 2008, **78**, 235104.
- 30 D. J. Temple, A. B. Kehoe, J. P. Allen, G. W. Watson and D. O. Scanlon, *J. Phys. Chem. C*, 2012, **116**, 7334–7340.
- 31 N. Aihara, K. Tanaka, H. Uchiki, A. Kanai and H. Araki, *Appl. Phys. Lett.*, 2015, **107**, 32101.
- 32 D. P. Halliday, R. Claridge, M. C. J. Goodman, B. G. Mendis, K. Durose and J. D. Major, *J. Appl. Phys.*, 2013, **113**, 223503.
- 33 J. P. Leitão, N. M. Santos, P. A. Fernandes, P. M. P. Salomé, A. F. da Cunha, J. C. González, G. M. Ribeiro and F. M. Matinaga, *Phys. Rev. B: Condens. Matter Mater. Phys.*, 2011, **84**, 24120.
- 34 L. Van Puyvelde, J. Lauwaert, P. F. Smet, S. Khelifi, T. Ericson, J. J. Scragg, D. Poelman, R. Van Deun, C. Platzer-Björkman and H. Vrielinck, *Thin Solid Films*, 2015, **582**, 146–150.
- 35 M. Grossberg, P. Salu, J. Raudoja and J. Krustok, *J. Photonics Energy*, 2013, **3**, 30599.
- 36 K. Maeda, *J. Phys. Chem. Solids*, 1965, **26**, 595–605.
- 37 J. J. Krustok, H. Collan and K. Hjelt, *J. Appl. Phys.*, 1997, **81**, 1442.
- 38 A. Aydinli, N. M. Gasanly and K. Göksen, *J. Appl. Phys.*, 2000, **88**, 7144–7149.
- 39 I. Repins, S. Glynn, J. Duenow, T. J. Coutts, W. K. Metzger and M. A. Contreras, *Proc. SPIE 7409, Thin Film Solar Technology*, 2009, 74090M, DOI: 10.1117/12.828365.
- 40 M. Birkett, PhD thesis, University of Liverpool, 2016.
- 41 E. G. Seebauer and M. C. Kratzer, *Charged Semiconductor Defects*, Springer London, London, 2009.
- 42 J. Krustok, A. Jagomagi, M. Grossberg, J. Raudoja and M. Danilson, *Sol. Energy Mater. Sol. Cells*, 2006, **90**, 1973–1982.